Spectral separability of bark beetle infestation stages: A single-tree time-series analysis using Planet imagery

Michele Dalponte [a,*], Ruggero Cetto [b], Daniele Marinelli [a], Davide Andreatta [a,c], Cristina Salvadori [b], Francesco Pirotti [d], Lorenzo Frizzera [a], Damiano Gianelle [a]

[a] Research and Innovation Centre, Fondazione Edmund Mach, via E. Mach 1, 38098 San Michele all'Adige, Italy
[b] Technology Transfer Centre, Fondazione Edmund Mach, via E. Mach 1, 38098 San Michele all'Adige, Italy
[c] Department of Agronomy, Food, Natural Resources, Animals and Environment, University of Padova, Viale dell'Università 16, 35020 Legnaro, Padova, Italy
[d] Department of Land, Environment, Agriculture and Forestry, University of Padova, Viale dell'Università 16, 35020 Legnaro, Padova, Italy

ARTICLE INFO

ABSTRACT

Bark beetles cause severe damage to European forests leading to impacts on many sectors, from the environmental to the economical. Timely mapping of the different stages of an attack is very important. Remote sensing has been widely used to map bark beetle damage using both airborne and satellite data. Newly available satellite multispectral data with a daily revisit time and high spatial resolution has the potential to monitor an attack in all its phases. This study explores the spectral separability of bark beetle infestation stages using the Planet imagery at individual tree level. Multi-temporal spectral analysis of 78 trees in different stages of a spruce bark beetle attack was carried out. Bands and vegetation indexes derived from 42 multispectral images were compared to eleven field surveys over a time span of approximately four months. The spectral separability analysis was done considering three criteria exploring: 1) the significance of the differences, 2) the magnitude of the differences and 3) the separability in a supervised classification context. The field surveys reported different effects depending on the season of the bark beetle attack - spring vs. summer. Spectral bands and indexes extracted from trees in the healthy and red-stage were significantly different. Trees in the green-attack stage at the end of the summer showed a statistically significant difference from healthy trees. The separability measured with a supervised classifier showed that it is possible to separate healthy, green-attack and red-stage trees with high accuracy values (kappa accuracy above 0.9).

1. Introduction

Bark beetles cause severe damage to European forests, and *Ips typographus* L. (Coleoptera: Curculionidae, Scolytidae) is the most damaging species (Hlásny et al., 2021). Bark beetle damage has increased by 700%, from 2.1 million of m³/year (1971/1980) to 14.5 million of m³/year (2002–2010), leading not only to environmental impact but also social and economic impact (Hlásny et al., 2019). In an equilibrium condition, called endemic phase, bark beetles have a role in the regeneration of ecosystem nutrients, but certain events (like windthrows) can trigger the beginning of the pandemic phase in the population. During this phase, insect populations can grow to the point where they can attack healthy plants, causing them to die (Mulock and Christiansen, 1986). *I. typographus* voltinism is composed of several broods whose number differs based on the climate region (Öhrn, 2012). In

North Italy at low altitudes, the insect might have the parental, first and the second brood but also several sister broods (Faccoli et al., 2000). The parental generation leaves the overwintering sites in spring (usually May), when the mean daily air temperature is about 18 °C (Annila, 1969) as it allows them to fly and find suitable hosts (*Picea abies* (L.) H. Karst.), whilst the other generations spread during the summer.

Infested trees are usually classified into three stages based on the crown colour: green-attack, red-stage and grey-stage. The crown colour turns in response to the bark beetle feeding process which affects the phloematic tissues. The green-attack stage represents the stage in which the tree has just been attacked by the bark beetle and it is still alive. Inside this stage the trees condition varies during the evolution of the infestation. The early-stage level of the green-attack is when the bark beetles first entered inside the tree: the tree is still alive and has started defensive processes against the parasite. The last level of the green-

attack is when the tree is already compromised and has begun either to have the first yellow needles or to experience some loss of green needles (Kautz et al., 2023). When the infestation is extensive around the stem and the tree is compromised, the crown will start to turn yellow and then red because of the loss of the tree conductive system. Grey stage is a decomposing stage, in which the dead tree loses its bark and needles. Only the green-attack stage is relevant for outbreak management as, at this stage, the trees are colonised by beetles before the developing brood leaves the tree.

The *I. typographus* control strategy depends on the purpose of the forest management. According to Hlásny et al. (2019), the principal method foresees two steps to be efficient: outbreaks individuation and logs treatment for killing the current brood. An early warning system is usually devised, based on the survey of pheromone traps placed in susceptible forest areas. Time-series of captured bark beetles are then used to develop short-term forecasting models which predict the risk areas (Šramel et al., 2021). To spatially map outbreaks, experienced staff are currently in charge of identifying from a distance the yellow/red crowns and *in situ* plants in green-attack stage. The efficiency of this method is very variable and impossible to replicate over large areas. For this reason, many studies have focused on detection methods based on remote sensing images. Senf et al. (2017), in a review study, summarise bark beetle detection methods using remote sensing data, concluding that most of the studies are based on multi-spectral data using spectral reflectance (47%), however 29% also used single spectral indices. Only 12% of the bark beetle studies are based on lidar data, and another 10% used hyperspectral imagery. Most studies with multispectral data are based on medium-resolution data (10–100 m), although a considerable proportion of them are with high-resolution data (1–10 m). In recent years many other studies have been carried out using satellite multi-spectral data to detect bark beetle damage at different scales (Luo et al., 2023). As bark beetle attacks happen at tree level, one important target for current and future studies is to work at individual tree scale. This requires high spatial and spectral resolution data that in the past were expensive and not easily accessible. Additionally, a target of current and future research should be the detection of the early stages of the attacks at single tree resolution. Newly launched high spatial resolution satellite constellations allow such kinds of studies, as for example the Dove constellation of Planet Labs Inc. allows an almost daily availability of images over an area with a spatial resolution of 3 m and 8 spectral bands.

The aim of this study is to explore the spectral separability of bark beetle infection stages at tree level over time. We analysed an area where field data collection was carried out for four months tracking the health status of each tree with an almost weekly time frequency. The spectral separability analysis was carried out using the Kruskal-Wallis statistical test, the Jeffries-Matusita distance, and the classification results obtained with a weighted Support Vector Machine classifier.

2. Materials

2.1. Study area and field data

The study area is located in the Autonomous Province of Trento (PAT) in Italy on the property of the municipality of Fornace, in locality Montepiano (Fig. 1). The area is at an altitude of 900 m a.s.l., with an almost plain morphology and volcanic geology. The area analysed is approximately 1 ha, mostly dominated by *Picea abies* (L.) H.Karst. and *Pinus sylvestris* L., with the minor presence of some other species like: *Abies alba* Mill., *Castanea sativa* Mill., *Fraxinus excelsior* L. and *Larix decidua* Mill.. The structure is even-aged and the forest renewal is mostly composed of broadleaved species or *A. alba*. During the last two decades (period 2002–2021) the threshold temperature of 18 °C, at which the bark beetle overwintering generation starts dispersal, has been reached between the end of March and the beginning of May, with a higher frequency at the middle-end of April (https://storico.meteotrentino.it/web.htm).
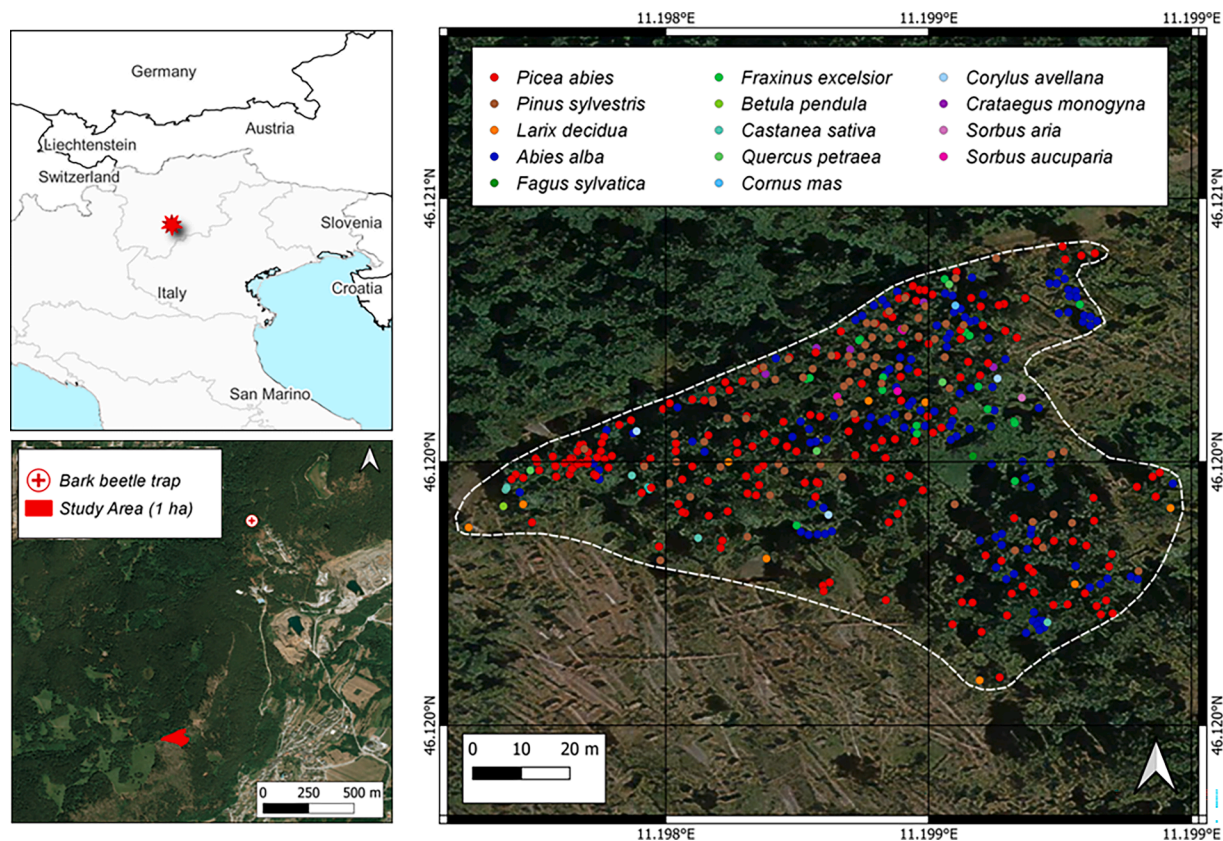

Fig. 1. Location of the study area, the background map in the detail image is from Bing imagery.

Between 27 and 29 October 2018, the forest in this area was hit by the Vaia storm. During the storm, precipitation was very severe fluctuating around 300–400 mm (Giovannini et al., 2021) with peaks of 800 mm, and winds reached peaks of 200 km/h. The storm massively impacted the forest in the area with significant windthrows damage (Chirici et al., 2019).

2.2. Field data

In this study we considered two types of field surveys: i) a bark beetle population monitoring survey using a pheromone trap, and ii) a tree health status monitoring survey. Both surveys were repeatedly conducted during summer, and autumn 2021.

The bark beetle population monitoring survey was done using a pheromone trap (included in the regional bark-beetle monitoring network) at 1.5 km distance from the study area (Fig. 1). An operator checked the trap with an almost biweekly frequency starting from 16 April 2021, counting the captured beetles (see Fig. 2). Bark beetles counts over time were used to predict the bark beetles flight curve and to understand population dynamics (swarming period, number of generations).

The tree health status monitoring survey was carried out at tree level on selected Norway spruce trees (147 trees). First, the position of each tree inside the 1 ha area was geolocated using a Lasertech TruePulse 360B starting from multiple base stations point localised with a precise GPS. Species, height, and diameter at breast height (DBH) of each tree with DBH higher than 5 cm were collected in the field: 425 trees, see Table 1. Subsequently, a subset of Norway spruce trees visible from satellite images, and well distributed over the plot, were selected (147 trees). The monitoring of the trees took place from 1 July-13 October 2021, on a bi-weekly basis approximately, except in July when it was weekly (Fig. 3). During the ground survey, the health condition of each selected tree was evaluated through a visual symptoms examination and attributed to one of the five health classes described in Table 2. It is worth noting that, with respect to the standard classification of healthy, green-attack, and red-stage, we split the green-attack stage into two subclasses (G1 and G2), and we added the yellowing class. Not all trees moved sequentially one class after another as in the time lapse between two surveys a tree could have progressed through more than one class.

2.3. Remote sensing data

Two remote sensing data sources were used in this study: satellite multispectral images (Dove images) and airborne lidar data. Dove is a constellation of more than 200 nano-satellites owned by the imaging company Planet Labs, Inc. (PlanetTeam, 2017), launched in 2017 and providing daily high resolution multi-spectral images. Though Planet is a commercial imaging company, many of its products are free for research purposes and they can be downloaded from their website (www.planet.com). The latest satellites of the constellation (SuperDove), used in this study, are able to acquire data in eight bands (Table 3). Each Dove image covers an area of 32.5 km × 19.6 km at 3.7 m ground sampling distance. All the level 3B images (orthorectified surface reflectance) at pixel size of 3 m acquired from 1 June to mid-October 2021 without cloud cover over the study area (91 images covering 58 days, Fig. 4) were downloaded. For some days multiple images were available. The surface reflectance was harmonized by Planet on the Sentinel-2 spectral values (Kington and Collison, 2022). As the study area was encompassed within a single Dove tile, there was no need for any image mosaicking.

Lidar data were acquired in 2015 by an Optech ALTM 3100EA sensor with a maximum scan angle of 21°. The mean point density was 21.5 points per square meter for the first return. Up to four returns per pulse were measured.

3. Methods

In Fig. 5 the architecture of the methodology adopted in this study is showed. In the following paragraphs the main steps are detailed.

Table 1
Summary of the trees measured in the field.

Species	Number of trees	DBH (cm)		
		Minimum	Mean	Maximum
Picea abies (L.) H.Karst.	178	5	32.5	65
Abies alba Mill.	119	5	8.4	24
Pinus sylvestris L.	69	28	40.3	57
Fraxinus excelsior L.	18	5	8.6	18
Larix decidua Mill.	9	29.5	46.4	56.5
Castanea sativa Mill.	8	6	10.6	17
Crataegus monogyna Jacq.	5	5	8.0	11
Sorbus aucuparia L.	4	7	10.2	13
Quercus petraea (Matt.) Liebl.	4	5	8.8	17
Corylus avellana L.	3	5	6.3	8
Sorbus aria (L.) Crantz	1	5	5.0	5
Fagus sylvatica L.	1	18	18.0	18
Cornus mas L.	1	5	5.0	5
Betula pendula Roth	1	10	10.0	10

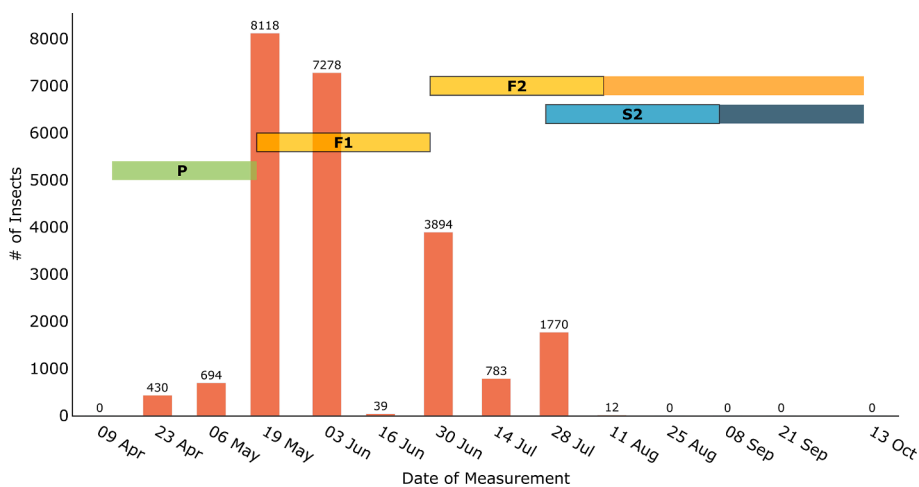**Fig. 2.** Pheromone trap data (number of insects caught) from the monitoring network (orange bars) and the development time of each brood of season 2021 (Parental/overwintering generation: P; first generation: F1; second generation F2; second sister brood S2). Development bars with black outline show brood growth with phloem feeding, development bars without black outline show periods of adults overwintering.
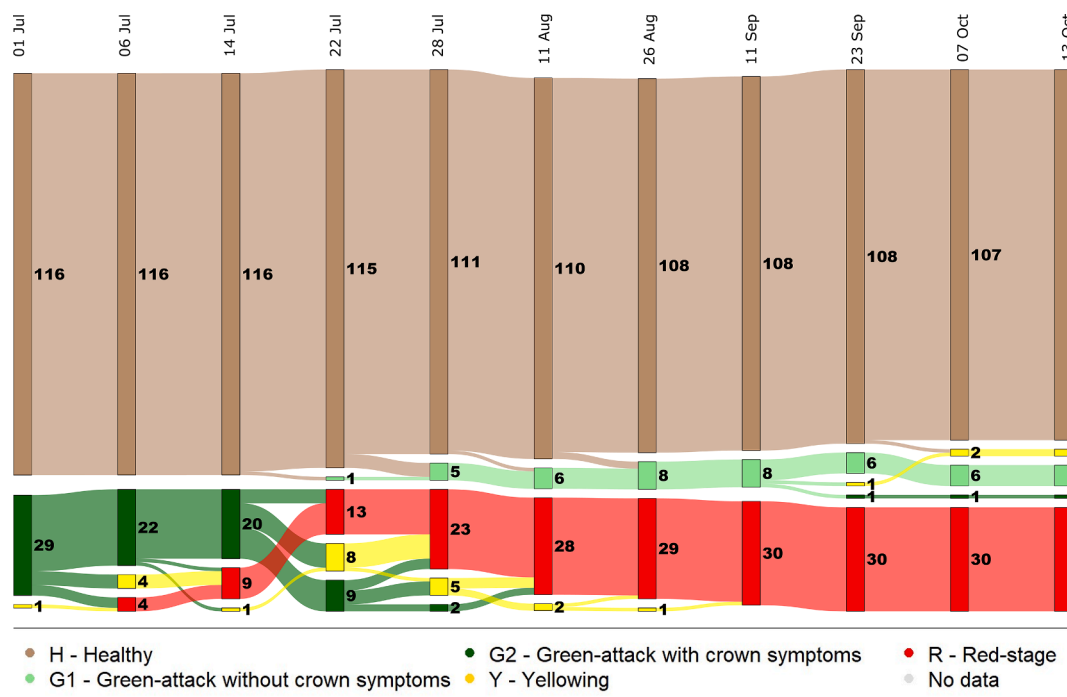
Fig. 3. Tree health status monitoring in the field. The numbers indicate the number of trees surveyed.

Table 2

Health status classification used in the field surveys.

Status	Description
H - Healthy	No entrance holes are visible from the ground even with the help of binoculars; there are no symptoms attributable to *I. typographus*.
G1 - Green-attack without crown symptoms	There are entrance holes with boring dust on the stem; no other symptoms are visible like needle losses, yellowish or reddish crown.
G2 - Green-attack with crown symptoms	There are entrance holes on the stem, sometimes also exit holes; in addition, there are needle losses with showy needleless branches; in some cases, it is possible to notice bark losses.
Y - Yellowing	There are entrance holes on the stem, sometimes also exit holes; the crown turns partially or totally yellow; in some cases, it is possible to notice bark losses.
R - Red-stage	There are entrance and exit holes; the crown has turned partially or totally red; in some cases, it is possible to notice bark losses.

Table 3

Dove spectral bands and comparison with the equivalent Sentinel-2 bands used for the data harmonization.[1]

Dove Name	Wavelength (FWHM) - nm	Sentinel-2 Name	Wavelength (FWHM) - nm	Resolution - m
B1 - Coastal Blue	443 (20)	B1 – Coastal Blue	442 (21)	60
B2 - Blue	490 (50)	B2 – Blue	492	10
B3 - Green I	531 (36)	–	–	–
B4 - Green II	565 (36)	B3 – Green	559 (36)	10
B5 - Yellow	610 (20)	–	–	–
B6 - Red	665 (31)	B4 -Red	664 (31)	10
B7 - Red Edge	705 (15)	B5 – Red Edge 1	704 (15)	20
B8 - Near-Infrared	865 (49)	B8A - Narrow NIR	864 (21)	20

[1] https://developers.planet.com/docs/apis/data/sensors/.

3.1. Lidar data processing

The lidar point cloud was normalized by subtracting the digital terrain model (DTM) from the z values of the lidar pulses. The DTM used was generated from the lidar points by the vendor using the TerraScan software with a grid size of 0.5 m. The Z normalization was carried out using the software *lasground* of the package LAStools (https://rapidlasso.com/). Lidar data were used in this study to delineate the individual tree crowns (ITCs). The delineation was carried out using the delineation algorithm of the R package *itcSegment* (Dalponte, 2018), in particular the function *itcLiDAR*. This is a region growing approach that uses both the point cloud and the rasterized lidar points. The method is based on two main steps: identification of the treetops, and detection of the crowns. The treetops are identified on a raster CHM generated from the point cloud. The identification is done using a variable size spatial moving window that identifies local maxima in the CHM. The strength of the method is to use a window size that varies according to the height of the central point of the window: higher values of the CHM give larger values of the window and vice versa. The crowns are then defined starting from the treetops using some rules with some parameters that are also driven by the height of the tree top. Finally, the lidar points of each delineated crown are extracted and the shape of the crown is defined according to the points distribution. A detailed description of the method adopted can be found in (Dalponte et al., 2018). To generate the ITCs dataset to use in the modelling part, a matching process between delineated ITCs and field measured trees was done. Euclidean distance between the position and height of the field measured trees and the ITCs was computed. Field measured trees were matched with an ITC if the Euclidean distance was lower than 3 m.

3.2. Dove images processing

The geolocation error of the Dove imagery is not constant and it could have a large variation image by image, thus we performed a geolocation accuracy analysis on the 91 Dove images available by comparing the position of a reference object in all the images. Images were then selected based on their geolocation accuracy. A road turn, at about 700 m from the study area, easily detectable in all the Dove
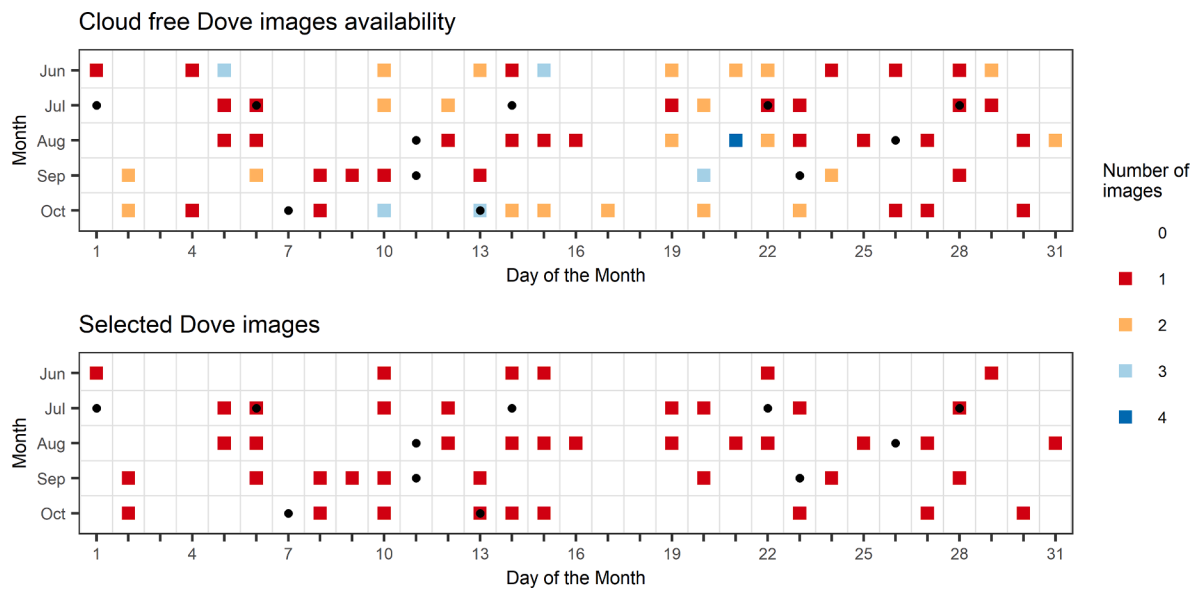
Fig. 4. Dates of the field surveys (black dots), acquisition dates of the cloud free Dove imagery and images frequency, and dates of the Dove images used in this study.
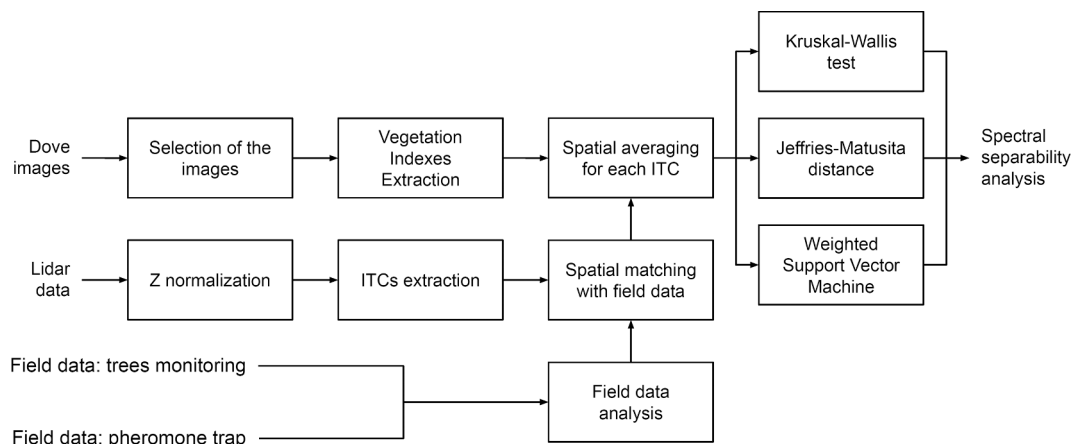

Fig. 5. Processing scheme adopted in this study.

images and near the study area was identified as a reference object. The reference road turn shape was manually delineated on a georeferenced very high resolution orthoimage (25 cm pixel spacing). Using an automatic delineation method based on image thresholding, the same road turn was automatically detected on all the Dove images (91 in this study). The 91 detected road turns were compared with the reference one considering three metrics: 1) the Jaccard index, that defines the level of overlap among two shapes; ii) the mean distance between the delineated border of the reference road turn and the border of the turn delineated on the Dove images; and iii) the maximum distance between the delineated border of the reference road turn and the border of the turn delineated on the Dove images. The distance between the border of the reference road turn and the border of the turn delineated on the Dove images was computed as follows: i) the detected road turn pixels were transformed into a shapefile following the border of the pixel patch defining the road turn; ii) the vertex points defining the shapefile were extracted; and iii) the distances of these points from the polygon of the reference turn were calculated using the R function *dist2Line*.

The images that had at least a Jaccard index of 0.5, a maximum distance below 6 m (two Dove pixels) and a mean distance below 3 m (one Dove pixel) were selected. For days for which multiple images were selected, the one with the highest Jaccard index was kept. The 91 road turns images, and their geolocation accuracy are reported in the

supplementary materials as Figure S1 and Table S1.

A series of vegetation indexes (VIs) were extracted from each Dove image selected (Table 4). Afterwards, for each matched ITC the weighted average of the pixels of the Dove bands/VIs were extracted. The weighted average was done based on the percentage of overlap of the ITC with the pixel. This resulted in a time-series of bands and VIs values for each matched ITC.

Radiometric calibration of Dove images is an issue as there could be large differences in spectral values according to the satellite that acquired the image (Frazier and Hemingway, 2021). As stated before, we chose the harmonized data and thus these issues are largely accounted for. To further reduce inconsistencies among different acquisitions, we applied a temporal filter to the time series of bands and VIs (Fakhri et al., 2022; Vidal and Amigo, 2012). Thus, the time-series were processed with a smoothing (low-pass) filter consisting in a moving window of size equal to 11 days, 5 days before and 5 days after each value and replacing the value with the average of the values falling inside the temporal window. As the image availability is not constant in time due to weather conditions and coverage of the Dove constellation, in each smoothing a different number of images was used depending on image availability in the 11-day time range.

Studies that involve long time series of images usually have to deal with possible radiometric drifts of the sensor. As this study spanned a

Table 4
Vegetation indices (VI), with formulas with Dove bands and references.

Index	Formula	Reference
GARI - Green Atmospherically Resistant Vegetation Index	$GARI = \dfrac{B8 - [B4 - (B2 - B6)]}{B8 - [B4 + (B2 - B6)]}$	(Gitelson et al., 2003)
GNDVI - Green Normalised Difference Vegetation Index	$GNDVI = \dfrac{B8 - B4}{B8 + B4}$	(Ahamed et al., 2011)
MCARI - Modified Chlorophyll Absorption Ratio Index	$MCARI = $ $[(B7 - B6) - (B7 - B4)] * \dfrac{B7}{B6}$	(Daughtry, 2000)
NDREI - Normalised Difference Red Edge Index	$NDREI = \dfrac{B8 - B7}{B8 + B7}$	(Hunt et al., 2011)
NDVI - Normalised Difference Vegetation Index	$NDVI = \dfrac{B8 - B6}{B8 + B6}$	(Huete and Jackson, 1987)
NRVI - Normalised Ratio Vegetation Index	$NRVI = \dfrac{\frac{B6}{B8} - 1}{\frac{B6}{B8} + 1}$	(Baret and Guyot, 1991)

period of only three and half months and it is quite unlikely that one sensor will be affected by such a problem, we did not consider it in our pre-processing.

3.3. Spectral separability analysis

The spectral separability of the five status classes in which the field trees were categorized was done considering three criteria exploring: 1) the significance of the differences, 2) the magnitude of the differences and 3) the separability in a supervised classification context (weighted Support Vector Machine classifier):

1. Kruskal-Wallis (KW) test: for each field data acquisition date, the nonparametric KW test was used to test if the band and index values at each sampling date were significantly different between the health status groups. The test was used to calculate pairwise comparisons between groups at each date. The goal of this procedure was to understand which stage of the infection was significantly different in terms of spectral information at each date. In each date only classes having at least 5 samples were considered.
2. Jeffries-Matusita (JM) distance: the JM distance (Bruzzone et al., 1995) is a parametric criterion widely used for feature selection (Dalponte et al., 2009). The JM distance considers the distance between class means and the distribution of values from the means. This is achieved by using the covariance matrices of the classes in the separability measurement. This separability criterion can be used to pairwise measure the separability between classes, and to evaluate the multiclass separability (Bruzzone et al., 1995). The values range between zero and the square root of two. In this specific case the JM distance was computed for each pair of classes in each date. In each date only classes having at least 5 samples were considered. Moreover, in each date the multiclass JM distance was computed for all the classes present in that date that had at least 5 samples.
3. Weighted Support Vector Machines (wSVM) classifier: for each date a wSVM classifier (Nguyen et al., 2019) was trained and validated using a leave-one-out cross validation strategy. We chose a Support Vector Machine classifier as it has been widely used for both tree species classification and bark beetle attack detection (Dalponte et al., 2022, 2009), and in particular, a weighted version in order to address the fact that for some health status classes we have very few samples. As for the previous cases, only classes having at least 5 samples were analysed. For each date, the best set of features was

selected using an exhaustive search strategy and, as separability measure, the kappa accuracy of the wSVM.

4. Results

4.1. Field data analysis

Analysing the results of the pheromone trap monitoring (Fig. 2) we saw that the swarming of the overwintering adults started in the first weeks of May 2021. After 6 May 2021, the parental generation swarmed and laid eggs, giving birth to the first generation. Eggs of the first generation develop in eight weeks (Kautz et al., 2023; Wermelinger and Seifert, 1998) and at the end of June they were developed adults ready to swarm and to lay the eggs of the second generation. The swarming peak on 28 July 2021 is likely a sister brood of the second generation.

Looking at the tree monitoring survey in relation to the pheromone trap analysis, we could see that the trees in the G2 class in July and R class in the following months could be related to the first generation, while the trees in the G1 class in August, September, and October to the second and the sister brood generations. Thus, between the attack of the beetles to a tree and the development of the first symptoms (green-attack) in the tree, there was a time span of approximately one month.

4.2. Image selection and ITCs delineation

The image selection procedure selected 42 images out of the 91 downloaded from the Planet website in the range 1 June 2021 – 30 October 2021 (Fig. 4). It is worth noting that for some days multiple images were available, and thus the number of days covered by the downloaded images was 58. The pool of selected images was characterized by an average Jaccard index of 0.591, an average mean distance of 1.476, and average maximum distance of 4.589 (See Figure S1 and Table S1).

The ITCs delineation procedure detected 363 ITCs over the 1 ha plot. Among them 156 matched a field measured tree, and among these trees 103 are Norway spruce. Among these Norway spruces 78 were monitored for their health status. The mean crown area of this last subset was 17.4 m^2, the median 16.0 m^2, the minimum 0.4 m^2, and the maximum 49.0 m^2.

4.3. Temporal signatures of bands and indexes

In Fig. 6 and Fig. 7 the temporal signatures of the bands and indexes are showed. The different classes behaved quite differently changing band/index. The separability among the healthy and bark beetle attacked trees increased, moving from June to October.

4.4. Kruskal-Wallis test

In Fig. 8 the results of the Kruskal-Wallis test are shown. Concerning the individual bands, the NIR band (B8) was the one where the difference among the health status groups was almost always not significant, especially in the second part of the season. The bands where the differences were more significant were B1 (coastal blue), B2 (blue) and B6 (red). The indexes that showed the most significant differences among the health classes were those based on the difference/ratio between near-infrared band and green band or red band: GNDVI, NDVI, and NRVI. Indices including blue and red-edge band (MCARI, GARI, and NDRE), on the other side, showed weaker significance for some class combinations. The difference among the groups healthy (H) and green-attack without crown symptoms (G1) were always significant except for 28 July 2021 (first day of appearance of this class) and for B8 and MCARI. MCARI showed no significant difference between H and green-attack with crown symptoms (G2). H and Y status were sampled together in two dates only and they demonstrated significant difference in all bands/VIs except for B8. H and R status were always significantly
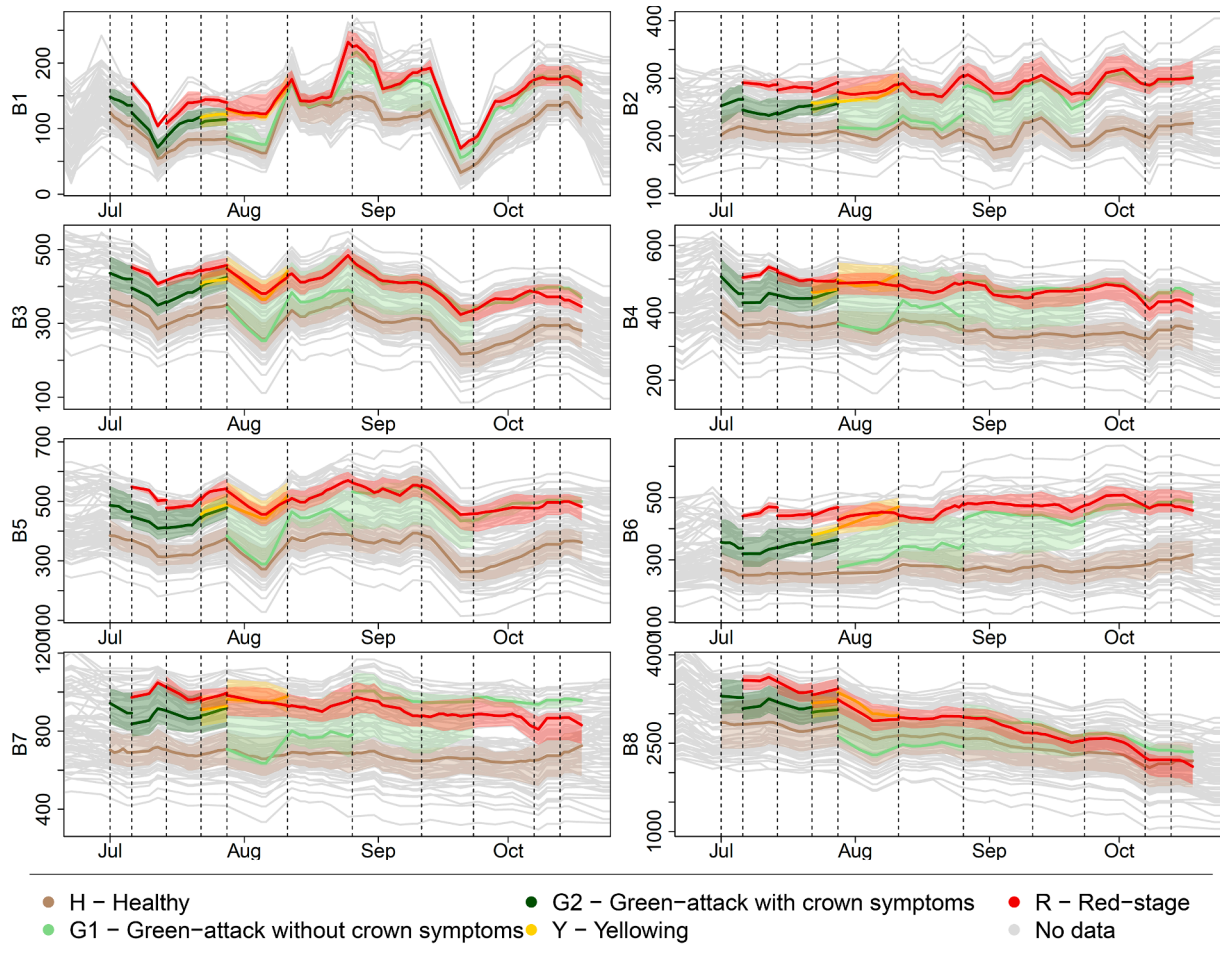
Fig. 6. Time-series of bands values for each sample tree (grey lines). Coloured lines (light brown, dark green, light green, yellow and red) represent the median value of each health status class and the tube around it the range of the 25th to the 75th percentile. The y values are reflectance values scaled by 10000.

different with a p-value below 0.01 for bands from 1 to 7 and all indexes, while for band 8 (NIR) they were not significantly different in the last field data acquisition dates (10–07, and 10–13). This could be related to autumnal phenological effects on the NIR band. G1 and R showed lower separability, being statistically different in band 2 (blue), band 6 (red), GNDVI, MCARI, NDVI, and NRVI. G2 and Y never showed a statistically significant difference except using MCARI, while G2 and R were significantly different using GNDVI, MCARI, NDVI, and NRVI. The difference among the groups yellowing (Y) and green-attack with crown symptoms (G2) was not significant except for MCARI (date: 22 July 2022), but the number of available samples for these two groups was quite low. On the same date, G2 and red-stage (R), and Y and R demonstrated low significant differences.

4.5. Jeffries-Matusita distance

In Fig. 9 the classes separability in each date measured with the Jeffries-Matusita distance are shown. Regarding the class combinations H - G1 and H - G2 the highest average separability was reached by GARI, and NDRE, while the lowest was shown by B8 and MCARI. H and Y were more separable using the indexes NDRE, GNDVI, NDVI, and NRVI, and less separable considering only the individual spectral bands. H and R classes were always the most separable reaching an average JM distance over the dates close or above 1 in almost all the cases. Only B8 and GARI showed low values of the distance. G1 and R were most separable using GNDVI, NDVI, NRVI, and MCARI, while B8, NDRE and B7 showed the least separability. MCARI showed to be the best index to separate G2 and Y classes, while again the individual bands showed the least separability.

Classes G2 and R were most separable using either NDVI or NRVI or GNDVI or B6 or MCARI, while NDRE and GARI showed very low separability.

Fig. 10 shows the multiclass JM distance for each date. In this case all the classes were considered on each date to compute the distances. Among the 11 sampling dates, 5 indexes provided the highest separability, and in particular NDVI in 5 dates out of 11, GARI and GNDVI in two dates out of 11 and B6 and MCARI in one date only.

The JM distance for the best five bands/indexes was plotted over time in Fig. 11 with respect to the most frequent 4 class combinations. As it can be seen for the combinations H-G1, H-G2 and H-R there was an increase in separability moving from July to October. For G1-R the behaviour was less stable, and it changes for each band/index.

4.6. Weighted Support Vector Machines classification

In Fig. 12 the kappa accuracy obtained with the wSVM at each date varying the number of features is shown. For all dates there is a saturation of the accuracy after 3 to 5 features, and a decrease in accuracy using all features. The dates are split into two groups, dates from 1 July-11 August, and dates from 26 August-13 October. For the first group the best kappa is in the range from 0.6 to 0.7 while for the second group it is above 0.8 (Fig. 12). B3, B4, and B8 were never selected in any date, and B5 and B7 only in two and one date respectively (Fig. 13). The most frequently selected feature was NDVI (10 dates) followed by MCARI (6 dates). B1, B2 and GNDVI were selected in 5 dates. The H and R classes always reached high classification accuracies in all survey dates (Table 5 and Table 6). The R class increased its classification accuracy moving
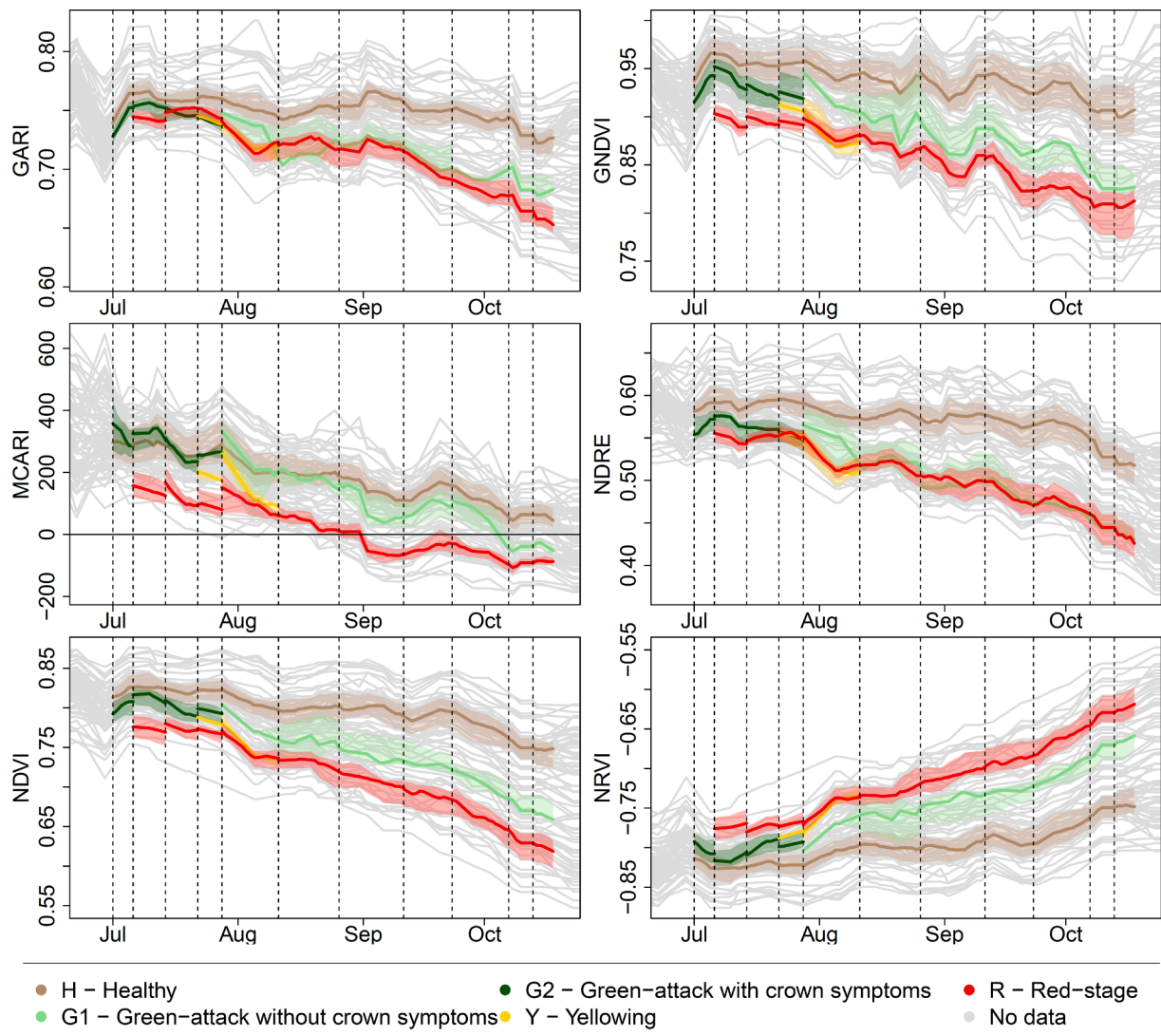
Fig. 7. Time-series of VIs values for each sample tree (grey lines). Coloured lines (light brown, dark green, light green, yellow and red) represent the median value of each health status class and the tube around it the range of the 25th to the 75th percentile.

from July to October. G1 and G2 classes reached good accuracies (above 80%) but in some dates the PAs and UAs were quite low (below 40%). Y class reached PA around 60% but lower UA. It is worth noting that the number of samples for the G1, G2 and Y classes was always quite small and thus the results were influenced by this.

5. Discussion

Based on the field data analysis, trees could have been clustered into three groups: i) trees that were not attacked by the bark beetles, ii) trees that were infested by the overwintering adults (parental generation) and damaged and killed by the larvae of the first generation, and iii) trees infested by the adults of the first generation and damaged by the larvae of the second and sister brood generations. It is worth noting that while most of the trees in the second group were in the R class in the last survey (13 October 2021), most of the trees in the third group were still in the G1 class at the end of the season. This behaviour was already observed before in the literature as reported by (Kautz et al., 2023; Wermelinger and Seifert, 1998). It is expected that the trees in the third group will move to the R class at the beginning of the growing season of the year after. Regarding the time span of each stage, there is not a fixed length as it depends on many factors, related to the attack density, tree resistance and temperature (Kautz et al., 2023).

The separation of the R status from the H status was quite clear as this status is clearly visible by the human eye. The separation of these two classes was possible in all the experiments considered: KW test, JM distance and wSVM classification. KM test showed that they are significantly different (p-value below 0.05) for all features and dates except for B8 in the last survey date; JM distance always showed high values, sometimes close to the saturation value; in the wSVM classification H reached PAs and UAs above 80%, while R was above 70% except for two dates. Many previous studies already showed the ability of remotely sensed data to detect the R stage from the H class (Huo et al., 2021; Luo et al., 2023). The distinction of the G1 and G2 groups from the H and R classes is normally a much more challenging topic (Huo et al., 2021). From the KM test and the JM distance G1 showed a clear distinction from the H status trees with the passing of time. These trees at the end of the season had spectral values much closer to the R class than to the H class. These results are confirmed by the wSVM results where it emerged that an automatic classification of H, G1 and R or H, G2 and R was possible and with high accuracy levels (but it also depends on the date). Both G1 and G2 classes reached PAs above 80%. The Y status seemed more difficult to separate from the G1, G2, and R status. The KW test showed that the separability between Y and G1, G2 and R was almost never significant (p-value above 0.1 in most of the cases), and similarly the JM distance showed low values for most of the features considered.

Dates (YYYY-MM-DD)	Classes pairs (trees number)	B1	B2	B3	B4	B5	B6	B7	B8	GARI	GNDVI	MCARI	NDRE	NDVI	NRVI
2021-07-01	H (53) - G2 (24)														
2021-07-06	H (53) - G2 (18)														
2021-07-14	H (53) - G2 (16)														
	H (53) - R (8)														
	G2 (16) - R (8)														
2021-07-22	H (52) - G2 (8)														
	H (52) - Y (6)														
	H (52) - R (11)														
	G2 (8) - Y (6)														
	G2 (8) - R (11)														
	Y (6) - R (11)														
2021-07-28	H (48) - G1 (5)														
	H (48) - Y (5)														
	H (48) - R (18)														
	G1 (5) - Y (5)														
	G1 (5) - R (18)														
	Y (5) - R (18)														
2021-08-11	H (48) - G1 (5)														
	H (48) - R (23)														
	G1 (5) - R (23)														
2021-08-26	H (46) - G1 (7)														
	H (46) - R (24)														
	G1 (7) - R (24)														
2021-09-11	H (46) - G1 (7)														
	H (46) - R (25)														
	G1 (7) - R (25)														
2021-09-23	H (46) - G1 (5)														
	H (46) - R (25)														
	G1 (5) - R (25)														
2021-10-07	H (45) - G1 (5)														
	H (45) - R (25)														
	G1 (5) - R (25)														
2021-10-13	H (45) - G1 (5)														
	H (45) - R (25)														
	G1 (5) - R (25)														

Legend:
- $0 <$ p-value ≤ 0.001
- $0.001 <$ p-value ≤ 0.01
- $0.01 <$ p-value ≤ 0.05
- p-value > 0.05

Fig. 8. Results of the Kruskal-Wallis test for each sampling date and for each health status classification available at each date. H = healthy; G1: green-attack without crown symptoms; G2: green-attack with crown symptoms; Y: yellowing; R: red-stage.

Nevertheless, in some features (in particular MCARI, NDVI and NRVI) a certain level of separability was detected by both KW test and JM distance, and indeed this was confirmed by the wSVM results where the Y class reached a PA of about 60%. The Y status is the least interesting from a management point of view as it is the beginning of the R status. We kept it in our analysis as it was field observed and moreover because it could be interesting to see how fast this status moves towards the R status.

In this study the identification of the most useful bands and indexes derived from the Dove data to separate back beetle infestation stages was done at two levels: in terms of individual bands/indexes using KM test and JM distance and considering groups of bands/indexes in a supervised classification context. Looking at the individual features, we can note that among the single spectral bands of the Dove images, the bands related to the chlorophyll absorption (i.e. B2 and B6) seemed to be impacted more by the bark beetle attack, while the NIR (B8) band seemed to be the least informative in separating the different health status classes. At the end of the summer season (September/October) the

Dates (YYYY-MM-DD)	Classes pairs (trees number)	B1	B2	B3	B4	B5	B6	B7	B8	GARI	GNDVI	MCARI	NDRE	NDVI	NRVI
2021-07-01	H (53) - G2 (24)														
2021-07-06	H (53) - G2 (18)														
2021-07-14	H (53) - G2 (16)														
	H (53) - R (8)														
	G2 (16) - R (8)														
2021-07-22	H (52) - G2 (8)														
	H (52) - Y (6)														
	H (52) - R (11)														
	G2 (8) - Y (6)														
	G2 (8) - R (11)														
	Y (6) - R (11)														
2021-07-28	H (48) - G1 (5)														
	H (48) - Y (5)														
	H (48) - R (18)														
	G1 (5) - Y (5)														
	G1 (5) - R (18)														
	Y (5) - R (18)														
2021-08-11	H (48) - G1 (5)														
	H (48) - R (23)														
	G1 (5) - R (23)														
2021-08-26	H (46) - G1 (7)														
	H (46) - R (24)														
	G1 (7) - R (24)														
2021-09-11	H (46) - G1 (7)														
	H (46) - R (25)														
	G1 (7) - R (25)														
2021-09-23	H (46) - G1 (5)														
	H (46) - R (25)														
	G1 (5) - R (25)														
2021-10-07	H (45) - G1 (5)														
	H (45) - R (25)														
	G1 (5) - R (25)														
2021-10-13	H (45) - G1 (5)														
	H (45) - R (25)														
	G1 (5) - R (25)														

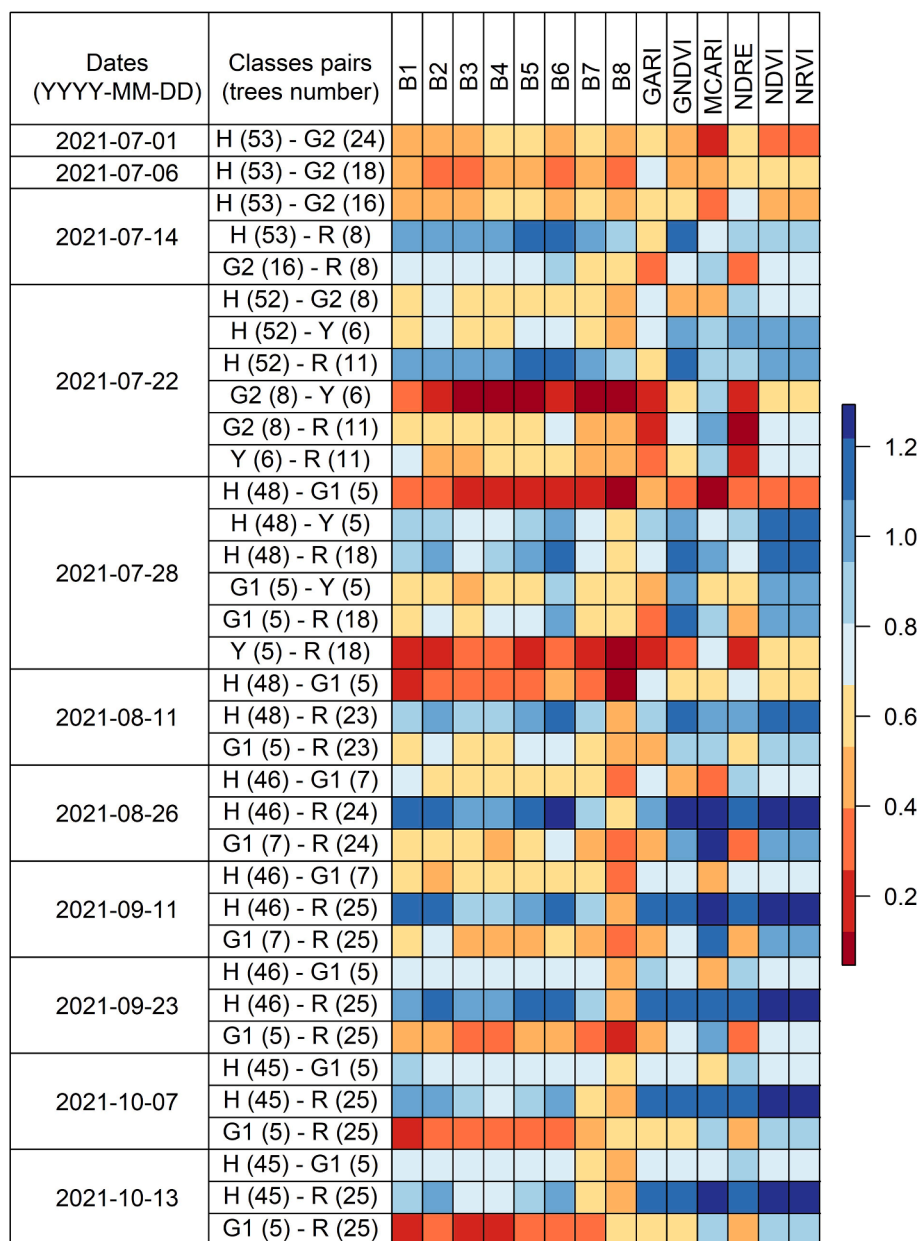**Fig. 9.** Jeffries-Matusita distance for each sampling date and for each classes pairs available at each date. H: healthy; G1: green-attack without crown symptoms; G2: green-attack with crown symptoms; Y: yellowing; R: red-stage.

values of the B8 band of the healthy and red-stage trees tend to overlap. These findings are similar to those of other studies, like (Bárta et al., 2022; Campbell et al., 2004; Lausch et al., 2013). It is well known that the NIR band of the spectrum is sensitive to the water content and structure of the vegetation thus probably the phenology that affects the trees approaching the autumn is influencing such results (Clevers et al., 2008; Hall et al., 1996). Considering the individual vegetation indexes the separation in terms of KM test and JM distance was quite clear in all indexes except for MCARI. GNDVI and NDRE showed a promising separability of H and G1 status trees. Similar results were obtained for G2, and in this case the distinction was much clearer using the NDRE index. This index is widely used and some other studies have pointed out that it could be used for early detection of bark beetle attacks (Abdullah et al., 2019).

In the wSVM classifications in each date, multiple features were considered. The features were selected considering an exhaustive search strategy and a leave-one-out validation. The features selected were

mainly spectral indexes, except for bands B1 and B2. These results are quite interesting as features carrying similar information were excluded: the spectral bands that are included within the spectral indexes were almost never considered while B1 and B2 that were not included in the indexes were frequently selected. Similarly, NRVI which is highly correlated with NDVI was selected fewer times compared to NDVI. It also emerged that a small number of features is enough to properly separate the health status classes considered in this study. It is worth noting that the results obtained in this study could be biased by the fact that a very small number of samples was available for some classes. This could have influenced the classification results but also the results obtained with the KW test and the JM distance.

When working with Dove data and bark beetle detection, four main issues should be considered: the area of the spectrum covered by the spectral bands, the spatial resolution, the spectral calibration of the bands among images of different days and satellites, and the low co-registration accuracy among images of different days and satellites.
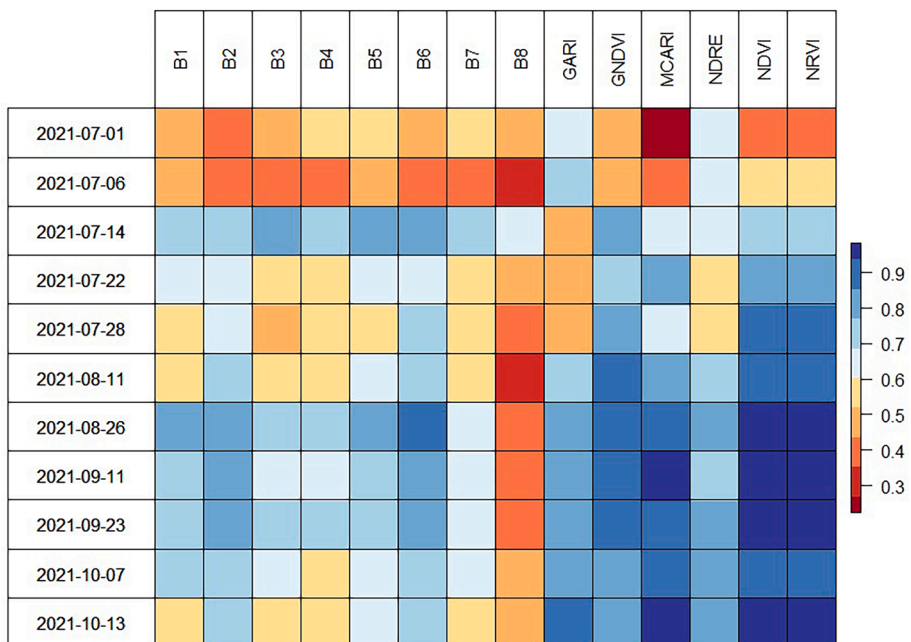
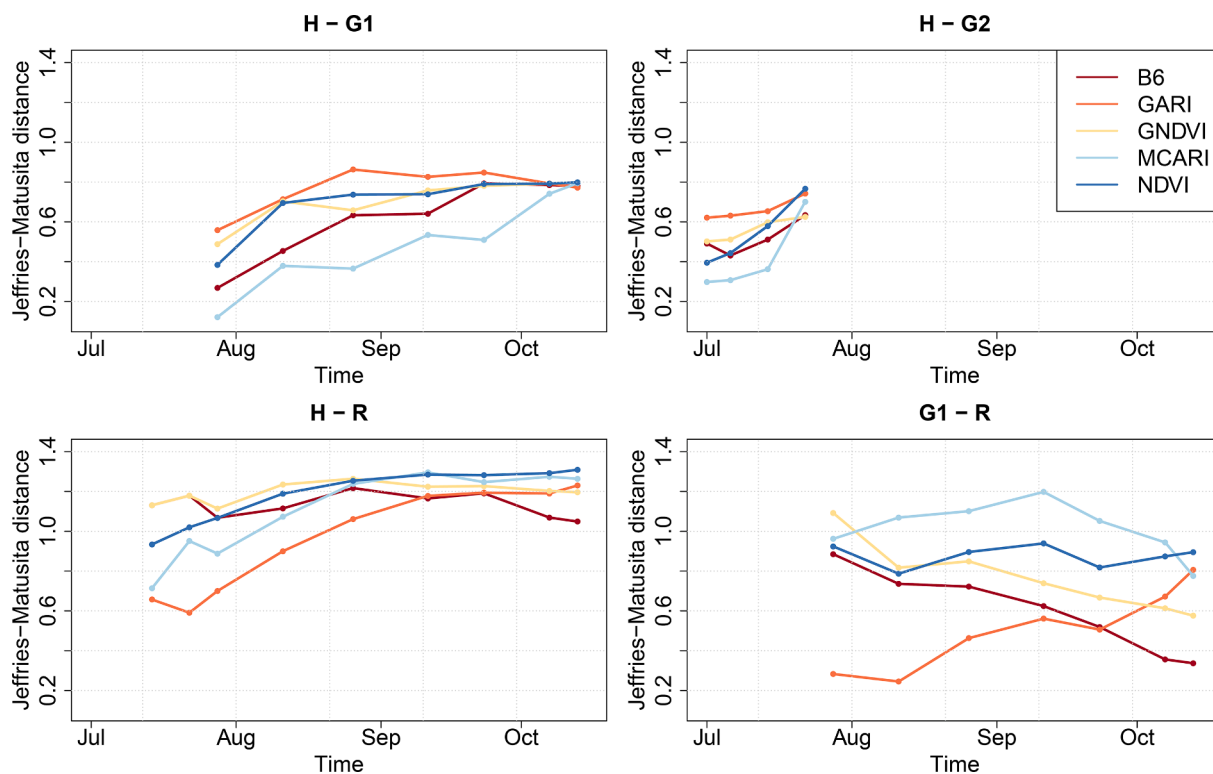**Fig. 10.** Multiclass Jeffries-Matusita distance for each sampling date.

Fig. 11. Jeffries-Matusita distance in time for the four most frequent classes combinations and the five band/indexes showing the highest separability. H: healthy; G1: green-attack without crown symptoms; G2: green-attack with crown symptoms; R: red-stage.

Dove images do not have any band in the SWIR part of the spectrum, which previous studies underlined as useful in early detection of a bark beetle attack (Huo et al., 2021). The limited number of bands of the Dove images is also limiting the number of vegetation indexes to extract. In this study we considered six vegetation indexes that mix the main bands of the Dove images, but other indexes could be extracted. A second limitation in using Dove images is the spatial resolution. Three metres spatial resolution is suitable when working with large trees but

too coarse for working with small trees. Dash et al. (2017) suggested 1 m as the optimal spatial resolution for monitoring forest health. In general, studies on object detection suggest that the optimal spatial resolution to detect an object should be four times less than the minimum object that one wants to detect (Hengl, 2006). Trees could be detected using other types of data, like lidar data, and then the individual tree crowns detected on lidar data could be intersected with satellite images (Dalponte et al., 2022). The spectral calibration of the bands is an issue in
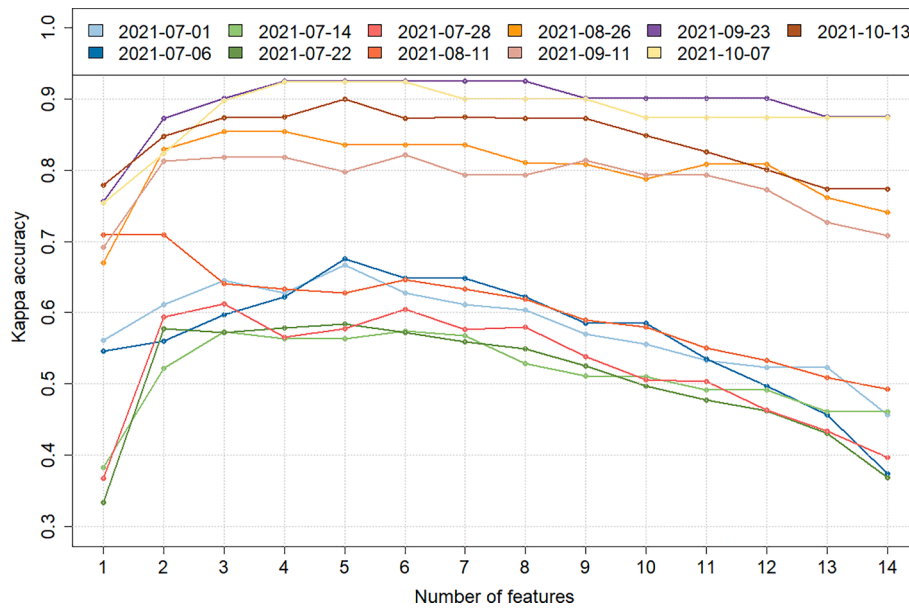
Fig. 12. Kappa accuracy varying the number of input features and the date.

Fig. 13. Best features selected in each date. The Gray square represents a selected feature.

Dove images as the constellation is made up by many satellites. In this study we dealt with this issue by considering the data with, (i) spectral bands harmonized on Sentinel-2 bands and, (ii) a smoothing of the spectral signatures. As shown in Fig. 6 for some bands there are some unstable behaviours even for the healthy trees. For bands 3 and 5 the most probable reason is to not be harmonized as there is not an equivalent Sentinel-2 band, and for band 1 to be harmonized on a band that has a 60 m resolution pixel. However, such bands are usually not used in the computation of the main spectral indexes used in vegetation studies and thus they could be excluded from the analysis. Regarding the problems in image co-registration in this study we decided to select images based on a reference object present inside the images instead of manually co-registering images to each other. This second approach could have resulted in better co-registrations and enabled the use of more images but at a much higher computational cost. Moreover, at 3 m resolution, it is not easy to detect individual trees and thus if a manmade object clearly visible in the area is not present this could result in issues with image selection and quality of the co-registration.

From this study, it emerged that there is the possibility to separate the H and R classes from the G1 and G2 classes. The separation between H and G1 spectral values is very useful as these trees from a visual inspection appear like the healthy ones, except for signs in the trunk bark. First generation and second sister brood development symptoms slowly appear from August to the next growing season, without any massive

Table 5
wSVM classification results for each date. Empty cells indicate missing data: that class was not present at that date or with a number of samples below 5. OA: overall accuracy; K: Kappa accuracy; BA: balanced accuracy; H: healthy; G1: green-attack without crown symptoms; G2: green-attack with crown symptoms; Y: yellowing; R: red-stage.

Date (YYYY-MM-DD)	OA	K	BA	Producer's accuracy					User's accuracy				
				H	G1	G2	Y	R	H	G1	G2	Y	R
2021–07-01	84.4	66.7	86.4	81.1	–	91.7	–	–	95.6	–	68.8	–	–
2021–07-06	85.9	67.6	88.7	83	–	94.4	–	–	97.8	–	65.4	–	–
2021–07-14	77.9	57.4	72.9	81.1	–	75	–	62.5	93.5	–	57.1	–	50
2021–07-22	77.9	58.4	64.1	88.5	–	37.5	66.7	63.6	93.9	–	33.3	40	77.8
2021–07-28	77.6	61.3	68.9	83.3	60	–	60	72.2	93	33.3	–	37.5	81.2
2021–08-11	85.5	70.9	59.5	95.8	0	–	–	82.6	93.9	0	–	–	82.6
2021–08-26	92.2	85.4	83.5	93.5	57.1	–	–	100	93.5	66.7	–	–	96
2021–09-11	89.7	82.2	90.2	84.8	85.7	–	–	100	97.5	50	–	–	96.2
2021–09-23	96.1	92.5	91.9	95.7	80	–	–	100	97.8	80	–	–	96.2
2021–10-07	96	92.4	91.9	95.6	80	–	–	100	97.7	80	–	–	96.2
2021–10-13	94.7	90	90.5	95.6	80	–	–	96	97.7	66.7	–	–	96

Table 6
Confusion matrices of the wSVM classifications for each date.

Date		H	G2
2021-07-01	H	43	2
	G2	10	22

Date		H	G2
2021-07-06	H	44	1
	G2	9	17

Date		H	G2	R
2021-07-14	H	43	2	1
	G2	7	12	2
	R	3	2	5

Date		H	G2	Y	R
2021-07-22	H	46	2	0	1
	G2	4	3	1	1
	Y	2	2	4	2
	R	0	1	1	7

Date		H	G1	Y	R
2021-07-28	H	40	2	0	1
	G1	6	3	0	0
	Y	1	0	3	4
	R	1	0	2	13

Date		H	G1	R
2021-08-11	H	46	3	0
	G1	0	0	4
	R	2	2	19

Date		H	G1	R
2021-08-26	H	43	3	0
	G1	2	4	0
	R	1	0	24

Date		H	G1	R
2021-09-11	H	39	1	0
	G1	6	6	0
	R	1	0	25

Date		H	G1	R
2021-09-23	H	44	1	0
	G1	1	4	0
	R	1	0	25

Date		H	G1	R
2021-10-07	H	43	1	0
	G1	1	4	0
	R	1	0	25

Date		H	G1	R
2021-10-13	H	43	1	0
	G1	1	4	1
	R	1	0	24

dispersal (see Fig. 3) and with very few trees turning from G1 to G2 and to R but with increasing spectral separability of the infected trees (G1 vs. H). This result could have a very important impact on management. G1 detection during early autumn could inform forest managers and allow the removal of G1 trees from forest, or support decisions regarding field activities such as cutting-debarking-chipping during the late-autumn and winter period to reduce the spread of the infestation.

It is worth noting that the clear separability between G1 and H trees was observed in a single study area and that only dominant trees were included to control for environmental, topographical and life-history traits which may affect vegetation spectral signature. Applying early detection models to detect bark beetle infestation on uneven forest stands in heterogeneous regions is more challenging. The results reported in this study can support the development of change detection algorithms for bark beetle detection at a larger scale. Such algorithms should account for seasonality cycles and for local context, analysing seasonal trends for change detection rather than working on raw value thresholding (Bárta et al., 2022). The contribution of this study to the open discussion on this complex topic was: to shed light on the importance of using the best spatial and temporal resolution available to track vegetation status at individual tree resolution, the analysis of spectral region relative importance for bark beetle detection, and the selection of the most informative vegetation indices. Moreover, we identified an ecological pattern which is worth mentioning in this context, since it may improve the design of monitoring systems for bark beetle early detection and forest management for limiting bark beetle spread. In our

study region the first brood of bark beetles impacts trees' health much faster than second and second sister broods. Slower symptom development and limited outbreak expansion to the nearest trees may allow an early green attack detection and infected plant removal during the autumn and winter period.

6. Conclusions

This paper analyses the spectral separability of bark beetle infestation stages using Planet imagery. The findings indicate that, while all stages can be distinguished with a high degree of accuracy, the separability varies depending on the time. Specifically, the green-attack stage (referred to as G1 and G2 in this study) and the red-stage (R) are more difficult to differentiate at the beginning of the season, but they become easier to distinguish towards the end of the season. On the other hand, healthy and red-stage trees are always easy to distinguish. We observed that symptom development in trees infected during the summer was slower than in other seasons, and that the spectral separability of healthy and green-attacked trees is highest in late summer, which was therefore identified as the best time to detect early green-attack. Early detection during late summer would enable the removal of infected plants during the autumn and winter months, reducing the next year outbreak potential at initial infestation stages.

Declaration of Competing Interest

The authors declare that they have no known competing financial interests or personal relationships that could have appeared to influence the work reported in this paper.

Data availability

The authors do not have permission to share data.

Acknowledgments

Appendix A. Supplementary data

Supplementary data to this article can be found online at https://doi.org/10.1016/j.ecolind.2023.110349.

References

Abdullah, H., Skidmore, A.K., Darvishzadeh, R., Heurich, M., Pettorelli, N., Disney, M., 2019. Sentinel-2 accurately maps green-attack stage of European spruce bark beetle (Ips typographus, L.) compared with Landsat-8. Remote Sens. Ecol. Conserv. 5 (1), 87–106. https://doi.org/10.1002/rse2.93.

Ahamed, T., Tian, L., Zhang, Y., Ting, K.C., 2011. A review of remote sensing methods for biomass feedstock production. Biomass Bioenergy 35, 2455–2469. https://doi.org/10.1016/j.biombioe.2011.02.028.

Annila, E., 1969. Influence of temperature upon the development and voltinism of Ips typographus L. (Coleoptera, Scolytidae). Ann. Zool. Fenn. 6, 161–208.

Baret, F., Guyot, G., 1991. Potentials and limits of vegetation indices for LAI and APAR assessment. Remote Sens. Environ. 35, 161–173. https://doi.org/10.1016/0034-4257(91)90009-U.

Bárta, V., Hanuš, J., Dobrovolný, L., Homolová, L., 2022. Comparison of field survey and remote sensing techniques for detection of bark beetle-infested trees. For. Ecol. Manage. 506, 119984 https://doi.org/10.1016/j.foreco.2021.119984.

Bruzzone, L., Roli, F., Serpico, S.B., 1995. An extension of the Jeffreys-Matusita distance to multiclass cases for feature selection. IEEE Trans. Geosci. Remote Sens. 33, 1318–1321. https://doi.org/10.1109/36.477187.

Campbell, P.K.E., Rock, B.N., Martin, M.E., Neefus, C.D., Irons, J.R., Middleton, E.M., Albrechtova, J., 2004. Detection of initial damage in Norway spruce canopies using hyperspectral airborne data. Int. J. Remote Sens. 25, 5557–5584. https://doi.org/10.1080/01431160410001726058.

Chirici, G., Giannetti, F., Travaglini, D., Nocentini, S., Francini, S., D'Amico, G., Calvo, E., Fasolini, D., Broll, M., Maistrelli, F., Tonner, J., Pietrogiovanna, M., Oberlechner, K., Andriolo, A., Comino, R., Faidiga, A., Pasutto, I., Carraro, G., Zen, S., Contarin, F., Alfonsi, L., Wolynski, A., Zanin, M., Gagliano, C., Tonolli, S., Zoanetti, R., Tonetti, R., Cavalli, R., Lingua, E., Pirotti, F., Grigolato, S., Bellingeri, D., Zini, E., Gianelle, D., Dalponte, M., Pompei, E., Stefani, A., Motta, R., Morresi, D., Garbarino, M., Alberti, G., Valdevit, F., Tomelleri, E., Torresani, M., Tonon, G., Marchi, M., Corona, P., Marchetti, M., 2019. Forest damage inventory after the "Vaia" storm in Italy. Forest@ - Rivista di Selvicoltura ed Ecologia Forestale 16, 3–9. https://doi.org/10.3832/efor3070-016.

Clevers, J.G.P.W., Kooistra, L., Schaepman, M.E., 2008. Using spectral information from the NIR water absorption features for the retrieval of canopy water content. Int. J. Appl. Earth Obs. Geoinf. 10, 388–397. https://doi.org/10.1016/j.jag.2008.03.003.

Dalponte, M., Bruzzone, L., Vescovo, L., Gianelle, D., 2009. The role of spectral resolution and classifier complexity in the analysis of hyperspectral images of forest areas. Remote Sens. Environ. 113, 2345–2355. https://doi.org/10.1016/j.rse.2009.06.013.

Dalponte, M., Frizzera, L., Ørka, H.O., Gobakken, T., Næsset, E., Gianelle, D., 2018. Predicting stem diameters and aboveground biomass of individual trees using remote sensing data. Ecol. Ind. 85, 367–376. https://doi.org/10.1016/j.ecolind.2017.10.066.

Dalponte, M., Solano-Correa, Y.T., Frizzera, L., Gianelle, D., 2022. Mapping a European Spruce Bark Beetle Outbreak Using Sentinel-2 Remote Sensing Data. Remote Sens. (Basel) 14, 3135. https://doi.org/10.3390/rs14133135.

Dalponte, M., 2018. Package ' itcSegment '.

Dash, J.P., Watt, M.S., Pearse, G.D., Heaphy, M., Dungey, H.S., 2017. Assessing very high resolution UAV imagery for monitoring forest health during a simulated disease outbreak. ISPRS J. Photogramm. Remote Sens. 131, 1–14. https://doi.org/10.1016/j.isprsjprs.2017.07.007.

Daughtry, C., 2000. Estimating Corn Leaf Chlorophyll Concentration from Leaf and Canopy Reflectance. Remote Sens. Environ. 74, 229–239. https://doi.org/10.1016/S0034-4257(00)00113-9.

Faccoli, Masutti, Baronio, 2000. Bioecologia di coleotteri scolitidi: Ips typographus (Linnaeus) e specie di recente interesse per la selvicoltura italiana dottorato di ricerca in entomologia agraria.

Fakhri, S.A., Valadan Zoej, M.J., Safdarinezhad, A., Yavari, P., 2022. Estimation of heavy metal concentrations (Cd and Pb) in plant leaves using optimal spectral indicators and artificial neural networks. Environ. Sci. Pollut. Res. 29, 76119–76134. https://doi.org/10.1007/s11356-022-21216-8.

Frazier, A.E., Hemingway, B.L., 2021. A Technical Review of Planet Smallsat Data: Practical Considerations for Processing and Using PlanetScope Imagery. Remote Sens. (Basel) 13, 3930. https://doi.org/10.3390/rs13193930.

Giovannini, L., Davolio, S., Zaramella, M., Zardi, D., Borga, M., 2021. Multi-model convection-resolving simulations of the October 2018 Vaia storm over Northeastern Italy. Atmos. Res. 253, 105455 https://doi.org/10.1016/j.atmosres.2021.105455.

Gitelson, A.A., Gritz †, Y., Merzlyak, M.N., 2003. Relationships between leaf chlorophyll content and spectral reflectance and algorithms for non-destructive chlorophyll assessment in higher plant leaves. J. Plant Physiol. 160, 271–282. https://doi.org/10.1078/0176-1617-00887.

Hall, F.G., Peddle, D.R., Ledrew, E.F., 1996. Remote sensing of biophysical variables in boreal forest stands of *Picea mariana*. Int. J. Remote Sens. 17, 3077–3081. https://doi.org/10.1080/01431169608949129.

Hengl, T., 2006. Finding the right pixel size. Comput. Geosci. 32, 1283–1298. https://doi.org/10.1016/j.cageo.2005.11.008.

Hlásny, T., Krokene, P., Liebhold, A., Montané-Huck, C., Müller, J., Qin, H., Raffa, K., Schelhaas, M.-J., Seidl, R., Svoboda, M., Viiri, H., European Forest Institute, 2019. Living with bark beetles: impacts, outlook and management options (From Science to Policy), From Science to Policy. European Forest Institute. https://doi.org/10.36333/fs08.

Hlásny, T., König, L., Krokene, P., Lindner, M., Montané-Huck, C., Müller, J., Qin, H., Raffa, K.F., Schelhaas, M.-J., Svoboda, M., Viiri, H., Seidl, R., 2021. Bark Beetle Outbreaks in Europe: State of Knowledge and Ways Forward for Management. Curr. Forestry Rep. 7, 138–165. https://doi.org/10.1007/s40725-021-00142-x.

Huete, A.R., Jackson, R.D., 1987. Suitability of spectral indices for evaluating vegetation characteristics on arid rangelands. Remote Sens. Environ. 23, 213-IN8. https://doi.org/10.1016/0034-4257(87)90038-1.

Hunt, E.R., Daughtry, C.S.T., Eitel, J.U.H., Long, D.S., 2011. Remote Sensing Leaf Chlorophyll Content Using a Visible Band Index. Agron. J. 103, 1090–1099. https://doi.org/10.2134/agronj2010.0395.

Huo, L., Persson, H.J., Lindberg, E., 2021. Early detection of forest stress from European spruce bark beetle attack, and a new vegetation index: Normalized distance red & SWIR (NDRS). Remote Sens. Environ. 255, 112240 https://doi.org/10.1016/j.rse.2020.112240.

Kautz, M., Peter, F.J., Harms, L., Kammen, S., Delb, H., 2023. Patterns, drivers and detectability of infestation symptoms following attacks by the European spruce bark beetle. J. Pest. Sci. 96, 403–414. https://doi.org/10.1007/s10340-022-01490-8.

Kington, Joe, Collison, Alan, 2022. Scene Level Normalization and Harmonization of Planet Dove Imagery.

Lausch, A., Heurich, M., Gordalla, D., Dobner, H.-J., Gwillym-Margianto, S., Salbach, C., 2013. Forecasting potential bark beetle outbreaks based on spruce forest vitality using hyperspectral remote-sensing techniques at different scales. For. Ecol. Manage. 308, 76–89. https://doi.org/10.1016/j.foreco.2013.07.043.

Luo, Y., Huang, H., Roques, A., 2023. Early Monitoring of Forest Wood-Boring Pests with Remote Sensing. Annu. Rev. Entomol. 68 (1), 277–298. https://doi.org/10.1146/annurev-ento-120220-125410.

Mulock, P., Christiansen, E., 1986. The threshold of successful attack by Ips typographus on Picea abies: A field experiment. For. Ecol. Manage. 14, 125–132. https://doi.org/10.1016/0378-1127(86)90097-6.

Nguyen, H.M., Demir, B., Dalponte, M., 2019. A weighted SVM-based approach to tree species classification at individual tree crown level using LiDAR data. Remote Sens. (Basel) 11 (24), 2948. https://doi.org/10.3390/rs11242948.

Öhrn, P., 2012. The spruce bark beetle Ips typographus in a changing climate - Effects of weather condition on the biology of Ips typographus. Europe; Revue Littéraire Mensuelle 18, 1–27.

PlanetTeam, 2017. Planet Application Program Interface. Space for Life on Earth.

Senf, C., Seidl, R., Hostert, P., 2017. Remote sensing of forest insect disturbances: Current state and future directions. Int. J. Appl. Earth Obs. Geoinf. 60, 49–60. https://doi.org/10.1016/j.jag.2017.04.004.

Šramel, N., Kavčič, A., Kolšek, M., Groot, M., 2021. Estimating the most effective and economical pheromone for monitoring the European spruce bark beetle. J. Appl. Entomol. 145, 312–325. https://doi.org/10.1111/jen.12853.

Vidal, M., Amigo, J.M., 2012. Pre-processing of hyperspectral images. Essential steps before image analysis. Chemom. Intel. Lab. Syst. 117, 138–148. https://doi.org/10.1016/j.chemolab.2012.05.009.

Wermelinger, B., Seifert, M., 1998. Analysis of the temperature dependent development of the spruce bark beetle *Ips typographus* (L) (Col., Scolytidae). J. Appl. Entomol. 122, 185–191. https://doi.org/10.1111/j.1439-0418.1998.tb01482.x.